Air circulation in deep fractures and the temperature field of an alpine rock slope

Jeffrey R. Moore*, Valentin Gischig, Maren Katterbach, and Simon Loew
Department of Earth Sciences
Swiss Federal Institute of Technology (ETH), Zurich, Switzerland
*contact: jeff.moore@utah.edu

Abstract

The subsurface temperature field of a rock slope is a key variable influencing both bedrock fracturing and slope stability. However, significant unknowns remain relating to the effect of air and water fracture flow, which can rapidly transmit temperature changes to appreciable depths. In this work, we analyze a unique set of temperature measurements from an alpine rock slope at ~2400 m a.s.l. in southern Switzerland. The monitored area encompasses part of an active slope instability above the village of Randa (VS) and is traversed by a network of open cracks, some of which have been traced to >80 m depth. We first describe distributed temperature measurements and borehole profiles, highlighting deep steady temperatures and different transient effects, and then use these data to approximate the conductive temperature field at the site. In a second step, we analyze the impact of air and water circulation in deep open fractures on the subsurface thermal field. On multiple visits to the study site in winter, we consistently noted the presence of warm air vents in the snowpack following the trace of deep tension cracks. Measurements showed that venting air changed temperature gradually from ~3 to 2 °C between December and May, which is similar to the rock temperature at around 50 m depth. Comparison with ambient air temperature suggests that winter conditions favor buoyancy-driven convective air flow in these fractures, which acts to cool the deep subsurface as the rock gives up heat to incoming air. The potential impact of this process on the local thermal field is revealed by a disturbed temperature profile in one borehole and transient signals observed at depths well below the thermal active layer. Seasonal water infiltration during snowmelt appears to have little impact on the temperature field in the monitored area.

Citation

Moore, J.R., V. Gischig, M. Katterbach, and S. Loew (2011). Air Circulation in Deep Fractures and the Temperature Field of an Alpine Rock Slope, *Earth Surface Processes and Landforms, 36*(15), 1985-1996.

1. Introduction

Thermal conditions in near-surface bedrock have, in recent years, gained a prominent role in alpine geosystems research. This is most evidenced in studies of mountain permafrost, where changes in the ground temperature distribution are increasingly implicated as a cause of anomalous slope failure activity in high alpine areas (e.g. Gruber and Haeberli, 2007). Observations attest, for example, to an exceptional number of rockfall events during the hot European summer of 2003, where massive ice could often be observed in detachment zones, suggesting a link between warming and rock slope destabilization through melting of cleft ice. As permafrost researchers delve further into the mechanisms governing rock fracture by ice segregation and volumetric expansion (see Matsuoka and Murton, 2008), and the frictional strength of ice-filled clefts (e.g. Davies et al., 2001), the need to understand the temperature field of alpine rock walls becomes increasingly critical.

Bedrock thermal conditions are not only of interest in permafrost settings. Many areas of the alpine landscape are subject to seasonal freezing conditions where mechanical weathering by ice may be an efficient mechanism of rock disintegration (Anderson, 1998). On a shorter time scale, daily temperature changes in near-surface bedrock can lead to grain-scale (and possibly greater) rock fracture and breakdown; so-called insolation weathering (Hall et al., 2008; McFadden et al., 2005). In addition to rock fracturing, the near-surface temperature field plays an important role in controlling Earth-atmosphere gas exchange, and terrestrial CO_2 and moisture flux (Weeks, 2001; Weisbrod et al., 2009; Kamai et al., 2009).

Heat conduction in a continuous bedrock volume is governed by the rock surface temperature distribution and geothermal heat flux (boundary conditions), and the diffusive properties of the medium (material properties) (Gueguen and Palciauskas, 1994; Wegmann et al., 1998). Rock surface temperatures can be approximated at the regional scale by considering surface energy fluxes, and the temperature distribution over a landscape estimated from climate and topographic data. Rock thermal diffusivity is controlled by the thermal conductivity and specific heat of the material, which can vary with moisture content, pore structure, and mineralogy, among other things. Combination of the rock surface temperature distribution with conductive heat flow modeling can be used to approximate the temperature field within representative mountain topography (e.g. Noetzli et al., 2007).

Real rock masses, however, present a number of discontinuities at different scales that act to disturb the conductive heat transfer system described above. One example is bedding or foliation, which can introduce anisotropic heat transfer properties. Here, however, we focus primarily on the implications of persistent fracture systems that can rapidly transmit water and air to appreciable depths in a rock mass. In the field of mountain permafrost research, the role of such fractures has been identified as a key unknown in understanding the mechanisms and rates at which rock walls respond to climate change (Gruber and Haeberli, 2007). Water circulation in cleft systems has been postulated, and in some cases observed to significantly affect the permafrost distribution at depth, creating thaw corridors and allowing rapid thaw penetration to depths not possible through conduction alone (Krautblatter and Hauck, 2007). Similarly, air flow and ventilation in talus slopes and rock glaciers has been shown to disturb the temperature distribution at depth, facilitating both rapid warming and cooling, and creating thermal anomalies (Delaloye and Lambiel, 2005; Phillips et al., 2009). Related engineering studies employ high-permeability embankment materials that encourage natural air convention and preserve underlying permafrost to avoid ground settlements (e.g. Goering and Kumar, 1996). In non-permafrost areas, near-surface fissures have been shown 'breathe' on both seasonal and daily time scales, taking in or exhausting air depending on relative density contrasts and the presence of local

convection cells (Weisbrod et al., 2009). Observations attest to wells that exhaust warm air for months in winter and have alternating exhaust and intake cycles during summer. Fracture systems also contribute to deep air circulation through an unsaturated rock mass, which can cause vadose zone drying and reduced fluid transport capacity (Weeks, 2001).

In this study, we address the impact of air and water fracture flow on the temperature field of an alpine rock slope at ~2400 m a.s.l. in southern Switzerland. We first approximate the conductive temperature field based on distributed measurements, highlighting deep steady temperatures and different transient effects. Then we discuss observations and mechanisms of convective disturbances by both air and water flow in deep fractures, and conclude by commenting on implications for rock slope instabilities.

2. Setting and temperature data

The monitored rock slope lies above the village of Randa in the Matter valley of southern Switzerland (Figure 1a). Steep topography reflects a rich history of glacial erosion, and is characterized by a typical deep inner valley trough with shoulders at the transition to more linear upper-valley slopes (Figure 1b). Maximum peak elevations are ~4500 m and adjacent valley floors ~1500 m, giving the area some of the greatest relief in the Alps. Primary lithologies in the upper portion of the rock slope are fine- to medium-grained paragneisses with bands of augengneiss and chlorite schist (Willenberg et al., 2008).

In spring 1991, two catastrophic rockslides released ~30 million m^3 of crystalline rock from the western wall above Randa. Following these events, a considerable rock volume remained unstable, and an extensive monitoring program was initiated. In 2001, three deep boreholes were drilled on a bench at the crown of the instability; two to 50 m depth (labeled sb50s and sb50n) and a third reaching 120 m (sb120) (Figure 1c, Figure 2). These boreholes were equipped with (among other things) piezometers and temperature sensors (together in a Geokon 4500 piezometer) in slotted inclinometer casings at their base (Willenberg et al., 2008). Piezometer measurements showed that the groundwater table is low within the instability, deeper than at least 120 m, while one local area of perched water was identified.

In 2008, the monitoring scheme was expanded to improve the spatial resolution of temperature measurements and explore thermal active layer conditions (i.e. the region above the zero annual amplitude (ZAA) depth where temperatures vary over the year). Two thermocouple arrays were installed in nearly flat lying ground (slightly south facing). The first extends to 4 m depth in intact rock and consists of nine thermocouples (Campbell Scientific 105E) at increasing spacing with depth (Figure 1c, Figure 2b). The second array lies in soil adjacent to the rock array, with five thermocouples extending to 0.5 m depth. This configuration allows us to monitor near-surface thermal conditions of both the bedrock and grassy soil that covers much of the crown area. Since a large portion of the rock slope is a steep, exposed cliff (scarp of the 1991 failures), we embedded a single thermocouple 50 mm into a nearby rock face with similar aspect. A number of additional temperature sensors are located within the crown area, attached to deformation monitoring equipment discussed in limited detail here. A meteorological station was also installed at the crown, measuring ambient air temperature (Campbell Scientific HMP45C – shielded and ventilated), relative humidity, barometric pressure, and summer rainfall (Figure 1c).

Boreholes sb50n and sb50s were selected for additional temperature measurements in August, 2010. The boreholes were filled with water and temperature profile logs conducted (since water slowly leaked out of the casings, they could not be filled to the top). We waited overnight to allow water temperature equilibration with the surrounding rock (also monitored with an in-place sensor), and then measured temperatures at 1 m increments.

Borehole sb50n could be reliably logged between 15 and 35 m depth, while sb50s was logged between 35 and 45 m. Also around this time, two portable sensors (Keller DCX-22, as used in the profile measurements) were deployed at different depths in the water-filled boreholes to measure temperature continuously over ~1 month intervals. In order to ensure accuracy and compatibility, these portable temperature sensors were calibrated in an ice-water bath.

Figure 3 summarizes temperature measurements at the site. Steady temperature at the base of the deepest borehole (120 m depth) has a long-term (2002 – present) mean value of 4.17 °C (Figure 3a). About 50 m horizontal distance from this borehole, the temperature at 50 m depth (sb50s) is constant at 3.47 °C. Steady temperatures at 31, 37, 41, and 43 m were measured to be 3.34, 3.45, 3.60, and 3.62 °C, respectively. Just 30 m horizontally from this borehole, the temperature at 50 m depth (sb50n) is 3.05 °C on average, but here shows a seasonal variation of ~0.2 °C peak to peak amplitude. Temperatures in this borehole are highest around the beginning of the year and lowest in early summer. A portable temperature sensor placed at 35 m depth measured a similar annual signal (see Figure 6c) with peak to peak amplitude of 0.4 °C. Temperature logs from boreholes sb50s and sb50n are shown in Figure 3a, together with data from short-term continuous measurements and long-term mean values of bottom-hole sensors.

At the base of the 4 m rock thermocouple array, the mean annual temperature (since 2008) is 5.8 °C, but strong seasonal variations of up to 7 °C (peak to peak) remain at this depth (Figure 3b,c). The mean annual temperature at the surface of the rock array is 5.5 °C, while the mean annual rock face surface temperature (southeast facing wall) is 6.1 °C. This difference arises because flat lying areas at the top of the slope are partially snow covered for nearly half the year, while the vertical rock faces remain snow free. Temperature sensors attached to crack extensometers Z9 and Z10 (Geokon model 4420) (see Figure 2b) show long-term mean values of 2.6 and 3.2 °C, respectively. Differences in mean surface temperatures over the study site illustrate the combined effect of variability in local micro-climate (e.g. incoming radiation, air temperature, humidity) and in-situ material properties (e.g. albedo, surface cover, thermal diffusivity). The mean annual air temperature (MAAT) measured since 2008 at 2360 m on the slope is 1.9 °C, with a typical annual amplitude of ~10 °C (Figure 3b,d).

On multiple visits to the study site in winter 2008-09 and 2009-10, we consistently noted the presence of warm air vents in the snow pack lying directly over deep tension cracks (Figure 4). The crown area is traversed by a network of fractures with varying widths and depths, many of which have been traced to ~50 m depth (one up to 85 m) with geophysical imaging to where they cross a borehole (Willenberg et al., 2008). The observed air vents were aligned with the trace of certain cracks (Figure 4a) and many remained in the same location from year to year. To further investigate the thermal conditions of these air vents, three thermistor dataloggers (Geotest UTL-3) were suspended into one crack at 0.5, 1.5, and 2.5 m depth. These were hung such that the sensing elements did not touch the rock walls or receive direct sun, so they measure crack air temperature. In addition, the temperature of air exiting all accessible vents was measured in January 2010 (Figure 4a), and thermal imagery confirmed the presence of warm air patches in the snowpack around the vents (Figure 4b,c).

The dense array and long time series of temperature measurements at this alpine rock slope provide a unique opportunity to understand the conductive temperature field, and investigate convective disturbances resulting from air and water flow in deep cracks. While the monitored slope is an active instability, we emphasize that the outcomes of this study are broadly applicable since all alpine rock slopes are fractured to some degree, and most have an extensive network of near-surface open fissures that can easily transmit both air and water.

3. Conductive temperature field

The conductive temperature field of a rock slope is governed by the diffusivity of the medium, thermal boundary conditions, and topography. Thermal diffusivity (α) can be calculated as $\alpha = \lambda C^{-1}$, where λ is thermal conductivity and C is the volumetric heat capacity. General values for rocks are $\lambda \sim 3$ W $m^{-1}K^{-1}$ and $C \sim$ 2E6 J $m^{-3}K^{-1}$, giving typical diffusivity of $\alpha \sim$ 1.5E-6 m^2s^{-1} (Gueguen and Palciauskas, 1994). The thermal diffusivity of in-situ Randa paragneiss could be estimated by solving the 1D heat diffusion equation for measured temperature forcing at the surface, and matching temperature data at depth from the 4 m deep rock borehole. This exercise yielded a diffusivity estimate of 2.0E-6 m^2s^{-1}, which is comparable to the generalized value above. Similar diffusivity estimation using data from the 0.5 m sensor array in soil yielded a value of 0.25E-6 m^2s^{-1}. Rock foliation creates anisotropic thermal conductivity with typical anisotropy ratios (parallel / perpendicular to fabric) of ~1.5 (Clauser and Huenges, 1995; Goy et al., 1996).

Distributed temperature measurements and diffusivity estimates were used to construct and calibrate a simplified, steady-state heat conduction model for the Randa rock slope. We used the commercial finite element software COMSOL Multiphysics to solve the heat transfer problem. Unknowns were: (1) the geothermal heat flux (lower boundary condition), (2) effective thermal diffusivity of the medium, and (3) the ground surface temperature distribution (upper boundary condition). They are described as follows:

1) The geothermal heat flux was estimated to be 75 mW m^{-2} from relevant values reported in the literature for the Swiss Alps (Rybach and Pfister, 1994; Wegman et al., 1998; Noetzli et al., 2007).

2) Heat conduction properties of the rock mass implemented in COMSOL were λ = 1.5 W $m^{-1}K^{-1}$ and C = 1.9E6 J $m^{-3}K^{-1}$, yielding diffusivity α = 7.7E-7 m^2s^{-1}. These values were found to provide best fit between modeled and measured borehole temperatures. The implemented diffusivity, however, is a factor of 2.5 lower than our calculated value. This difference may be caused by the strongly-fractured rock mass within the instability (up to 17% air-filled void space was predicted from geophysical measurements by Heincke et al., 2006) or by air and water circulation, which create lower apparent diffusivity than for intact rock.

3) To determine the ground surface temperature distribution, two parameters are needed: (a) the mean ground surface temperature (MGST) at a known elevation, and (b) the variation of MGST with altitude. MGST at the monitored slope is highly heterogeneous depending on aspect, ground cover and shading, and for this exercise we need both a spatial and temporal mean. We evaluated all measured temperatures from in-situ sensors, and assume that MGST is typically ~1 °C greater than the MAAT (Goy et al., 1996) and less than measured temperatures at depth. Mean temperatures recorded by crack extensometers provided the best estimate of MGST, despite these sensors not directly measuring ground temperature (they are covered and lie a few mm above rock). MGST at 2350 m was thus estimated to be 2.6 °C. Rybach and Pfister (1994) review data from Switzerland regarding variation of MGST with altitude, and report an average value of -5 °C km^{-1}. This is consistent with the local air temperature lapse rate, which we measured to be -5 °C km^{-1} between the town of Randa and the monitored area (930 m altitude difference).

Table 1 summarizes input parameters for the heat conduction model used to produce the best fit with measured borehole temperatures at Randa.

The modeled steady-state conductive temperature field for the mountain profile is shown in Figure 5a, while a detail of the monitored area is shown in Figure 5b. The modeled temperature distribution is similar to other reported cases for alpine rock slopes (e.g.

Noetzli et al., 2007), and the 0 °C isotherm is located at an altitude of 2880 m consistent with predicted permafrost occurrence (BAFU, 2006). Temperature estimates near the peak are less reliable since a different surface temperature distribution on the opposing slope face was not considered. Figure 5c shows modeled steady temperatures along a simulated borehole through the center of the monitored area compared with measured values. Good fit could be achieved between the 2D isotropic model and temperature data from logs in the two 50 m deep boreholes. Notable deviations are also evident, especially in sb50n where the temperature log shows a cooling trend at ~30 m depth. Temperatures measured at the base of the boreholes could not be matched precisely with the same model fitting the temperature logs. This may be due to: a) lack of calibration between the different sensor types (it is not possible to access the bottom-hole sensors), or b) localized disturbances to the temperature field as in sb50n. The same model parameters used to match temperatures in the upper ~100 m of the rock mass were used throughout the entire model as no data are available regarding variation of rock mass thermal properties with depth.

Anisotropic heat transfer properties were implemented and the results compared against the 2D isotropic case. Thermal conductivity parallel to foliation (nearly horizontal in our section; Figure 1) was increased to 2.25 W $m^{-1}K^{-1}$, while perpendicular to foliation the value was kept as modeled above (anisotropy ratio = 1.5). Figure 5c compares isotropic and anisotropic models against measured temperatures along a simulated borehole. The effect of implementing anisotropic thermal conductivity was found to be relatively minor; only a slight deviation from the isotropic case can be observed (<0.5 °C at 100 m). We cannot say which model is more appropriate, so for simplicity we retain isotropic heat transfer properties throughout the remainder of this work.

The study area includes steep 3D topography, and the instrumented site sits on a ridge trending perpendicular to the main valley. Three dimensional effects on the temperature field are created by both geometry and changes in insolation with aspect. Here we simply explore the role of geometry, ignoring the influence of aspect which is potentially strong but poorly constrained. We kept the surface temperature forcing the same as in the 2D models (only a function of altitude), and created a new independent 3D model of the instrumented area. The resulting steady-state temperature field is represented along the simulated borehole in Figure 5c, and compared to the 2D isotropic and anisotropic cases. Results demonstrate a notable influence of 3D geometry, where rock at depth is cooler by >1 °C at 100 m compared to the 2D isotropic case. Heat transfer is generally more efficient in steep 3D topography as a point at the interior of the body has an overall shorter average distance to the ground surface (Noetzli et al., 2007).

Temperature time history data are shown in Figure 3d for the rock face, rock surface at the top of the shallow array, soil surface, and ambient air sensors. Each can be approximated as a sinusoid by fitting mean temperatures and cycle amplitudes; an annual amplitude of 10 °C was found to best match our data. The transient ground surface temperature distribution as a function of time (t) and elevation (z) could thus be approximated as:

$$T(t,z) = 2.6 + 0.005 * (2350 - z) + 10\sin(2\pi ft) \qquad (1)$$

where t is in seconds, z is meters a.s.l., and f is the one-year cycle frequency in Hz. Using this ground surface temperature forcing, we next explore transient effects and thermal active layer dynamics at the site.

Transient ground temperature profiles for winter (Jan. 1), spring (Apr. 1), summer (Jul. 1), and fall (Oct. 1) are shown in Figure 6a, and together with measured borehole temperatures in Figure 6b. Diffusive heat transfer in the thermal active layer (i.e. region above the ZAA) modifies temperatures up to 15 m depth, where the annual variation falls below 0.1 °C (1% of the surface amplitude). In summer, the warming front propagates

downward, heating bedrock at shallow depth while the deeper portion is still below the mean temperature due to the previous winter cooling. Equation 1 can also be modified to express daily temperature variations. Based on in-situ measurements, we maintain the same amplitude as for annual variations (10 °C), and resolve a daily thermal active layer thickness in the range of 0.8 m for rock. Using the measured diffusivity of soil, the daily thermal active layer thickness decreases to 0.4 m. Note these values are not the characteristic diffusion length scale (distance needed to decay to 1/e of the surface amplitude); calculated length scales are 2.8 m for an annual signal and diffusivity of the rock mass, and 0.15 and 0.08 m for a daily signal and diffusivity of rock mass and soil, respectively.

4. Convective disturbances

Temperature data and simulated profiles shown in Figure 6 illustrate a key difference between boreholes sb50n and sb50s. Despite them being only ~30 m apart, the temperature logs show a significant deviation in sb50n around 25 to 35 m depth, while the upper portion of the log together with data from sb50s fits the simulated conductive temperature profile well. As a result, we can identify a disturbed portion of borehole sb50n and calculate the local magnitude of this disturbance to be ~0.3 °C. Borehole sb50s, on the other hand, appears undisturbed with a temperature profile predicted well by a purely conductive model. Conductive heat transfer alone is not able to reproduce the observed disturbance in borehole sb50n (without some additional heat sink), and similarly cannot explain the presence of an annual signal at 35 and 50 m depth in this borehole. Only an advective process, able to rapidly transmit fluid to these depths, can create the observed annual trend. Here we explore disturbances to the Randa temperature field by water and air convection in deep fractures.

4.1. Water flow in fractured rock

Water circulation in fractured rock masses is commonly implicated to explain anomalous temperatures at depth in underground excavations or drillings. Generally deviations tend towards lower temperatures, implying infiltration of cooler surface water (Rybach and Pfister, 1994; Goy et al., 1996). While most of our instrumented rock slope appears to be dry (piezometer measurements show no water in boreholes sb120 and sb50n), one borehole (sb50s) has a seasonal water influx at the time of snowmelt amounting to ~1 m of pressure head. We suspect there is a local pocket of perched groundwater around the borehole (Willenberg et al., 2008). The water pressure increase is rapid (a few weeks), and pressure then decays slowly over the remainder of the year. Temperature measurements from a sensor embedded in the piezometer at the bottom of borehole sb50s, however, show steady conditions with no annual signal, and the temperature log between 35 and 45 m appears undisturbed (Figure 6b). Together, these observations suggest that seasonal water infiltration does not significantly modify the local temperature field around the borehole.

Annual temperature signals are observed in (dry) borehole sb50n at depths of 35 and 50 m (Figure 6c), however these do not match the expected variation for snowmelt infiltration. Specifically, temperatures reach a maximum value around December of each year and begin to decrease in January even when very little snowmelt has occurred. For snowmelt, we expect a rapid temperature decrease at affected depths beginning at the onset of melt in late spring followed by rebounding temperatures throughout the year. There is, on close examination, a slight temperature decrease at 50 m depth that occurs each year near the time of snowmelt, which may be related to water infiltration. At this same time, however, temperature at 35 m depth has already begun to increase.

At least for the monitored area of the slope, our data indicate that temperature disturbances by infiltrating water are relatively minor. The area may be anomalously fractured and dry because of the ongoing instability movement, and we cannot comment on the role of water infiltration in areas where we have no data. We do consider it likely, however, that overall subsurface temperatures are slightly depressed owing to efficient snowmelt infiltration through the fractured rock mass.

4.2. Air circulation in deep cracks

Cracks and boreholes penetrating a fractured rock mass have been shown to efficiently circulate air on both daily and seasonal time scales, depending on the temperature contrast between the in-situ rock and atmosphere (Weeks, 2001; Weisbrod et al., 2009). Similarly, natural passageways of coarse blocks in talus slopes can act as chimneys allowing air convection under certain atmospheric conditions (Delaloye and Lambiel, 2005; Phillips et al., 2009). At the Randa study site, we have observed convective air flow by the presence of warm air vents in the snowpack during winter. Such vents were found to exhaust warm and humid air, and typically had a ring of hoar crystals growing nearest the center. Air flow was not sufficiently fast to be felt or measured, but looking on one vent sideways we could distinguish visual distortion due to warm air rising from the crack. Figure 3a displays a map of observed vents in January 2010, highlighting their correlation with mapped open cracks. The temperature of venting air was also measured and found to vary between ~1 to 4 °C (while ambient air temperatures were in the range of -8 to -2 °C), which is similar to the rock temperature at depths of ~10 to 100 m. Warm air vents appear preferentially aligned with steeply-dipping cracks showing opening mode displacement, some of which have been traced up to 80 m depth and have aperture at the surface of ~0.5 m (Willenberg et al., 2008). Figure 3c shows a thermal image of the monitored area from the same time, confirming the presence of warm air in the snow around the vents. One vent in the center of the monitored area was selected for observation and instrumented with thermistor data loggers measuring air temperature. A complete annual time history for these sensors is shown in Figure 7a.

The temperature of air inside the monitored crack exhibits an interesting annual trend (Figure 7a): in summer, large temperature fluctuations are observed which mimic atmospheric air temperature changes and are typical of diffusive heat transfer (Figure 7d), while in winter crack air temperatures hold steady at around 3 °C for nearly eight months. Steady winter temperatures are occasionally interrupted during particularly warm or windy periods (Figure 7c). On close inspection, the crack air temperature is observed to change gradually over the winter from ~3 to 2 °C. This temperature change likely reflects cooling of some body of rock at depth that has given up heat to entering atmospheric air. Crack air temperature usually varies systematically with depth, where the lowest sensor is coolest and the upper sensor is warmest both in summer and winter. This variation is expected for both diffusive (conductive) heat exchange in summer and also convective air venting in winter.

We distinguish three hypotheses regarding the origin of convective fracture flow:

1) Local air convection cells develop within a sufficiently wide and deep crack (as in Weisbrod et al., 2009). During winter, air at depth is warmer than atmospheric air and the resulting density contrast drives localized convection cells. Cool atmospheric air descends into the fracture, warms and is expelled in another area along the trace of the crack. Winter conditions favor pervasive circulation, while in summer convection cells may form only at night or not at all. The same phenomenon can also occur on a daily period. Crack aperture required to support free convection may be as small as 10 mm (Kamai et al., 2009). Similar localized convection is exploited to cool permafrost ground

underlying gravel embankments, and is there referred to as the 'thermal diode' (Goering and Kumar, 1996).

2) Warm air within the rock mass is lighter than the same column of cool air outside (in winter), and the resulting pressure difference causes atmospheric air to invade the rock mass at lower elevations, become warmed and expelled to the atmosphere at higher elevations. Such a convection cell can be thought to exist half inside the rock mass and half in the atmosphere. Steep topography and a permeable rock mass are required for this process to be effective. Nearly continuous circulation is again expected during winter. The same mechanism drives natural ventilation of mines (see Weeks, 2001) and ventilation of coarse talus deposits (e.g. Delaloye and Lambiel, 2005), and is referred to as the 'topographic' or 'chimney' effect.

3) Barometric pressure changes stimulate air flow within a permeable rock mass (termed 'barometric pumping'). Under rising pressure conditions, air pressure within the rock is lower than atmospheric and air enters the rock mass. Under falling pressure, the internal air pressure is higher and a connected crack would vent air. The time scale of this effect is controlled by the period of barometric pressure changes and the permeability of the rock mass. For most rock masses, pressures equilibrate rapidly (~1 hour reported by Weeks, 2001) and the effect is considered of minor importance. At Randa, we observe nearly in-phase correlation (<60 min. offset) between dry borehole piezometer data from 120 m depth and atmospheric pressure, suggesting high pneumatic permeability and rapid equilibration.

While we can rule out barometric pumping on a seasonal time scale, we cannot conclusively identify the origin of cool air in our idealized crack convection cell. For local convection within the crack, air flow originates at the nearby ground surface, while for the topographic effect air flow enters the rock mass through the cliff face somewhere below. We consider both mechanisms feasible at the Randa study site. The rock mass is heavily fractured over several hundred meters, and the scarp of the 1991 rockslides forms a high cliff, so air flow from the face is possible. On the other hand, localized convection cells are equally feasible and have been observed at similar fractures even in the absence of steep topography (Weisbrod et al., 2009). By adopting local convection cells we can quantitatively address the observations using Rayleigh number analysis, which as shown below reveals promising trends with recorded crack air temperatures.

Conditions favoring free convection within an idealized crack (smooth and parallel walls) can be predicted by the Rayleigh number (R), which describes the ratio of buoyant forces to the product of thermal and momentum diffusivities:

$$R = \frac{\Delta\rho g k L}{\alpha \eta} \qquad (2)$$

Here $\Delta\rho$ is the density difference between atmospheric and crack air over a length L, k is the fracture permeability (estimated from mean aperture using the cubic law), and η is the dynamic viscosity of air. Buoyancy-driven flow (free convection) is predicted when the Rayleigh number exceeds a critical value, typically assumed to be $4\pi^2$ or ~40 (Nield, 1982; Weisbrod and Draglia, 2006).

Using recorded air temperatures at the site, we were able to calculate a Rayleigh number time history for our monitored crack. We assume L = 30 m and that the temperature at this depth is steady at 3 °C. We also assume a lower-bound mean crack aperture of 10 mm, giving permeability k = 8E-6 m^2. Calculated Rayleigh number as a function of time can be seen in Figure 7b, where values greater than the critical indicate convection conditions and values less than the critical suggest conduction conditions (stable air stratification and diffusive heat transfer). Good correlation can be observed between the

Rayleigh number trend and recorded crack temperatures: crack air temperatures stabilize under convective conditions (Figure 7c), while they follow air temperature under conductive conditions (Figure 7d). On the seasonal time scale, convection is pervasive throughout winter, while in spring and fall alternating convection and conduction conditions occur due to periodic warming and cooling. Each significant warming brings the predicted onset of conductive heat transfer, and crack air temperatures mimic the outside air temperature until successive cooling again favors convection and air circulation. In summer, conductive conditions prevail, and crack air temperatures gradually rise with large daily variations. These results are relatively insensitive to changes in the assumed crack geometry.

Air circulation in deep cracks will disturb the purely conductive temperature field predicted in Section 3. Convective circulation during winter cools the deep subsurface as rock gives up heat to the incoming air (as supported by our crack air temperature measurements), while potentially warming the near-surface region as air rises in cracks. Figure 6b highlights deviations in the temperature profile of borehole sb50n that cannot be explained by either steady or transient heat conduction models. Specifically, between 25 and 35 m depth the temperature log reverses gradient and cools. Since we can rule out the effect of snowmelt infiltration (at least locally), this disturbance is most likely caused by winter-time crack air circulation. Similarly, revisiting transient signals observed in the same borehole at 35 and 50 m depth (Figure 6c), we find an annual trend that cannot be explained by heat conduction or snowmelt infiltration. Rather, we note that the onset of cooling at 35 m occurs in December, just as convective venting is predicted at our nearby monitored crack (Figure 7b). Temperature trends at 35 and 50 m suggest cooling closer to the upper sensor; the onset of cooling at 50 m is delayed by >1 month and the amplitude is about half the value observed at 35 m. Examining the borehole logs (Willenberg et al., 2008), we find a steep actively-opening crack crosses the borehole at ~22 m, and a loss of cuttings into the rock mass was noted in this same region during drilling. However, we see no air vents around the area of extrapolated surface expression. We did map vents aligned with crack Z10 just behind the instrumented borehole (Figure 2b), which is one likely source of the observed cooling. The geometry of the suggested ventilation cell cannot be conclusively identified at this time.

The spatial variation of temperature disturbances created by crack air flow will be highly heterogeneous depending on the geometry of developed convection cells. We envision a number of opposing and repeating convection cells along the strike of an idealized crack, where each vent in the snowpack accommodates exiting air flow from two adjacent cells. The true geometry of the convection cells will depend on the crack geometry both along strike and at depth, but our field observations suggest that air vents in the snow cover occur roughly every 10 m (Figure 4), which would then also be the predicted order of length scale for convection cells. Air flow descends into the crack through the snowpack, which has high pneumatic permeability. Quantitative prediction of the cooling effect on the deeper rock mass remains a task of future numerical simulation, potentially coupling a heat conduction model with buoyancy-driven convective crack air flow in 3D. Such a model might also be extended for transient simulation taking seasonal crack wall temperature variations into account. An additional point to be addressed would be the role of crack air humidity and vapor flux, which could have a significant influence on the net energy balance and cooling of the crack walls by evaporation (Kamai et al., 2009; Weisbrod et al., 2009).

5. Implications for rock slope deformation

In related work at Randa, Gischig et al. (2011) demonstrated that near-surface thermo-elastic stress changes were transmitted to depths below the thermal active layer and provided seasonal stress cycles on critically stressed discontinuities; the so-called thermo-

mechanical (TM) effect. They showed that the Randa rock slope is particularly sensitive to TM stress changes, and that seasonal trends in the instability's displacement rate could be explained by TM forcing. However, one observation that remained unexplained was the apparent trend where the entire instability appears to react almost instantaneously to near-surface temperature changes; i.e., deformation rates increase synchronously each year in fall when ground temperatures drop. Coupled TM modeling allowing only transient heat conduction showed that the onset of acceleration could vary at different depths. The question remained, does the instability react as one or are the field observations simply a coincidence?

Convective air flow in cracks may provide the mechanism to transmit temperature changes to appreciable depths in the rock mass, and thus allow the instability to react synchronously when temperature conditions cross a critical threshold. In the preceding analysis, we showed how convective crack circulation is predicted essentially when the mean air temperature falls below the mean crack temperature at depth. The onset of convective venting brings cold atmospheric air penetrating to depths of ~10 to 50 m, cooling the rock mass below the thermal active layer. This cooling induces a thermo-elastic response in the nearby rock that results in stress redistribution throughout the connected medium, and which may cause the entire instability to deform. The effect of convective crack flow is to allow temperature changes, and thus induced stress changes, to propagate rapidly and synchronously to depth.

Figure 8 compares the computed Rayleigh number to in-place inclinometer data from a monitored discontinuity at 12 m depth in borehole sb120. Inclinometer data are filtered and the long-term linear trend is subtracted to highlight annual variations; positive slopes imply a rate increase with respect to the average, negative slopes a rate decrease. Good correlation can be seen between the predicted onset or end of convection and discontinuity deformation rate (Figure 8b,c). In fall, the dislocation rate increases just as crack convection begins, while the opposite occurs in early summer when the rate decreases as crack convection comes to an end. Short-term variations in dislocation rate also correlate with predicted crack air circulation. During summer, several week-long cold periods bring on convective air flow and inclinometer data show concurrent accelerations. In general, the onset of convection correlates with observed increases in discontinuity dislocation rate, lending support to the hypothesized feedback between convective cooling at depth, induced thermo-mechanical stress changes, and instability deformation.

6. Conclusions

We have collected and analyzed a comprehensive set of temperature measurements from the Randa rock slope in southern Switzerland with the aim of: 1) constructing a model of the conductive temperature field at the site, and 2) highlighting the role of convective disturbances caused by water and air flow in open fractures. Borehole and surface temperature data allowed calibration of a 2D transient-conductive thermal model, which was then used to explore effects of anisotropy and 3D topography. Diffusivity calculated from intact rock could not be applied directly in the model as it did not account for the lower thermal conductivity of the fractured rock mass. Fractured rock with high pneumatic permeability was confirmed by comparing deep borehole and ambient air pressures, which showed rapid equilibration implying efficient air flow in the rock mass. Measured borehole temperature logs revealed disturbed portions of the subsurface thermal field, where temperatures were cooler than predicted by conductive heat transfer models. The role of infiltrating snowmelt was found to be negligible in the monitored area (at least on the annual time scale), as shown by complementary borehole piezometer and temperature measurements; no temperature changes were observed during snowmelt even as head

increased by ~1 m. On the other hand, we have shown that favorable conditions for buoyancy-driven convective air flow in fractures prevail throughout winter, while in summer stable air stratification exists in the cracks and diffusive heat transfer dominates. We hypothesized a model of winter-time crack convection where air descends into the open fracture through the snowpack, becomes warmed by the rock at depth, and then is expelled at vents. Field observations and temperature measurements revealed unambiguous identification of such warm air vents, which were also visualized with thermal imagery. The temperature of venting air in mid-January ranged from 1 to 4 °C (while ambient air temperature was around -8 °C), which is similar to the temperature of rock at around 10 to 100 m depth. Clues as to the impact of this convective air flow on the subsurface thermal field are apparent in borehole temperature measurements, which showed both disturbed regions and transient signals at depths below the thermal active layer. Crack air convection provides a means to rapidly transmit cooling fronts to depths of >10 m, which in the case of the Randa rock slope instability may also influence the temporal displacement trend.

We emphasize that the outcomes of this study are not strictly limited to slope instabilities, since all alpine rock slopes are fractured to some degree. Although discontinuity systems in bedrock are ubiquitous, predicting the occurrence of discrete open fractures penetrating to depths of more than ~10 m remains a challenging task. Such fractures are commonly present in both active and inactive rock slope instabilities (as evidenced by many case studies), but can also occur throughout the alpine landscape in association with, e.g. fault zones, post-glacial relaxation strains, and differential weathering. In this work, we demonstrated that air circulation in deep, open fractures can create temperature anomalies at depth, with mean temperatures tending to be cooler than expected (a result also supported by recent work of Hasler et al., 2011). Winter-time air circulation removes heat from the rock mass, which is not reversibly replaced in summer – a thermal diode. This outcome implies that simplified models of subsurface rock temperatures may be subject to significant error, as would any analyses of physical processes based on these temperatures, e.g. bedrock fracturing by ice lens growth or slope destabilization by cleft ice melting. However, we point out that while the spatial distribution of discrete fractures able to support air circulation may be difficult to assess *a priori*, there may exist a predictable temporal pattern of air temperature gradients that either drive or prevent crack circulation: convection commences essentially when the mean ambient air temperature at the surface drops below the mean temperature at the bottom of the crack (or where the crack closes). Therefore, with *a priori* estimates of mean rock temperatures at depth, and readily available ambient air temperature data, the temporal occurrence of convective conditions could be predicted, and times of thermal disturbance explored in relation to mechanisms of bedrock fracturing and slope destabilization.

Acknowledgements

The authors wish to thank T.C. Hales and an anonymous reviewer for comments that improved and clarified this manuscript. Thanks to Kerry Leith and Keith Evans for many insightful discussions, and to Andreas Rubin and Prof. Jan Carmeliet from the Chair of Building Physics (Department of Architecture, ETH Zurich) for use of the thermal camera. Bettina Schäppi from the Chair of Hydrology and Water Resources Management (ETH Zurich) supplied relevant air temperature data from the village of Randa. Funding was provided in part by the Swiss National Science Foundation and by the Competence Center for Environment and Sustainability (CCES) of the ETH domain.

References

Anderson RS. 1998. Near-surface thermal profiles in alpine bedrock: implications for the frost weathering of rock. Arctic Alpine Res. **30**: 362-372.

BAFU (Hrsg.). 2006. Übersicht über die potenzielle Permafrostverbreitung in der Schweiz. Bern.

Clauser C, Huenges E. 1995. Thermal conductivity of rocks and minerals, Rock Physics and Phase Relations. AGU: 105-126.

Davies MCR, Hamza O, Harris C. 2001. The effect of rise in mean annual temperature on the stability of rock slopes containing ice-filled discontinuities. Permafrost Periglac. Process. **12**: 137-144.

Delaloye R, Lambiel C. 2005. Evidences of winter ascending air circulation throughout talus slopes and rock glaciers situated in the lower belt of alpine discontinuous permafrost. Norsk geogr. Tidsskr. **59**: 194-201.

Gischig V, Moore JR, Evans KF, Amann F, Loew S. 2011. Thermo-mechanical forcing of deep rock slope deformation - Part II: the Randa rock slope instability. J. Geophys. Res. 2011JF002007.

Goering DJ, Kumar P. 1996. Winter-time convection in open-graded embankments. Cold Regions Science and Technology **24**: 57-74.

Goy L, Fabre D, Menard G. 1996. Modelling of rock temperatures for deep alpine tunnel projects. Rock Mech. Rock Engng. **29**: 1-18.

Gruber S, Haeberli W. 2007. Permafrost in steep bedrock slopes and its temperature-related destabilization following climate change. J. Geophys. Res. **112**: doi:10.1029/2006JF000547.

Gueguen Y, Palciauskas V. 1994. Introduction to the physics of rocks. Princeton University Press: Princeton, NJ.

Hall K, Guglielmin M, Strini A. 2008. Weathering of granite in Antarctica: II. Thermal stress at the grain scale. Earth Surf. Process. Landforms **33**: 475-493.

Hasler A, Gruber S, Haeberli W. 2011. Temperature variability and thermal offset in steep alpine rock and ice faces. The Cryosphere Discuss. **5**: 721-753.

Heincke B, Maurer H, Green AG, Willenberg H, Spillmann T, Burlini L. 2006. Characterizing an unstable mountain slope using shallow 2D and 3D seismic tomography. Geophysics **71**: B241-B256.

Kamai T, Weisbrod N, Dragila MI. 2009. Impact of ambient temperature on evaporation from surface-exposed fractures. Water Resour. Res. **45**: W02417, doi:10.1029/2008WR007354

Krautblatter M, Hauck C. 2007. Electrical resistivity tomography monitoring of permafrost in solid rock walls. J. Geophys. Res. **112**: F02S20, doi:10.1029/2006JF000546.

Matsuoka N, Murton J. 2008. Frost weathering: recent advances and future directions. Permafrost Periglac. Process. **19**: 195-210.

McFadden LD, Eppes MC, Gillespie AR, Hallet B. 2005. Physical weathering in arid landscapes due to diurnal variation in the direction of solar heating. GSA Bulletin **117**: 161-173.

Nield DA. 1982. Onset of convection in a porous layer saturated by an ideal gas. Int. J. Heat Mass Transfer **25**: 1605-1606.

Noetzli J, Gruber S, Kohl T, Salzmann N, Haeberli W. 2007. Three-dimensional distribution and evolution of permafrost temperatures in an idealized high-mountain topography. J. Geophys. Res. **112**: F02S13, doi:10.1029/2006JF000545.

Phillips M, Zenklusen Mutter E, Kern-Luetschg M, Lehnig M. 2009. Rapid degradation of ice in a ventilated talus slope: Fluela Pass, Swiss Alps. Permafrost Periglac. Process. **20**: 1-14.

Rybach L, Pfister M. 1994. Temperature predictions and predictive temperatures in deep tunnels. Rock Mech. Rock Engng. **27**: 77-88.

Weeks EP. 2001. Effect of topography on gas flow in unsaturated fractured rock: Concepts and observations, in Flow and Transport Through Unsaturated Fractured Rock. Geophys. Monogr. Ser., **42**: D.D. Evans, T.J. Nicholson, T.C. Rasmussen Eds., 53-59.

Wegmann M, Hilmar Gudmundsson G, Haeberli W. 1998. Permafrost changes in rock walls and the retreat of alpine glaciers: a thermal modeling approach. Permafrost Periglac. Process. **9**: 23-33.

Weisbrod N, Draglia MI. 2006. Potential impact of convective fracture venting on salt-crust buildup and ground-water salinization in arid environments. Journal of Arid Environments **65**: 386-399.

Weisbrod N, Dragila MI, Nachshon U, Pillersdorf M. 2009. Falling through the cracks: The role of fractures in Earth-atmosphere gas exchange. Geophys. Res. Lett. **36**: L02401, doi:10.1029/2008GL036096.

Willenberg H, Loew S, Eberhardt E, Evans KF, Spillmann T, Heincke B, Maurer H-R, Green A. 2008. Internal structure and deformation of an unstable crystalline rock mass above Randa (Switzerland): Part I – Internal structure from integrated geological and geophysical investigations. Eng. Geol. **101**: 1-14.

Table 1: Model parameters used to calculate the 2D conductive temperature field.

Thermal conductivity (λ)	1.5 W m^{-1} K^{-1}
Volumetric heat capacity (C)	1.9E6 J m^{-3} K^{-1}
Thermal diffusivity (α)	7.7E-7 m^2 s^{-1}
Conductivity anisotropy ratio	1.5
MGST at 2350 m	2.6 °C
Variation of MGST with elevation	-5 °C km^{-1}
Geothermal heat flux	75 mW m^{-2}
Annual temperature cycle amplitude	10 °C

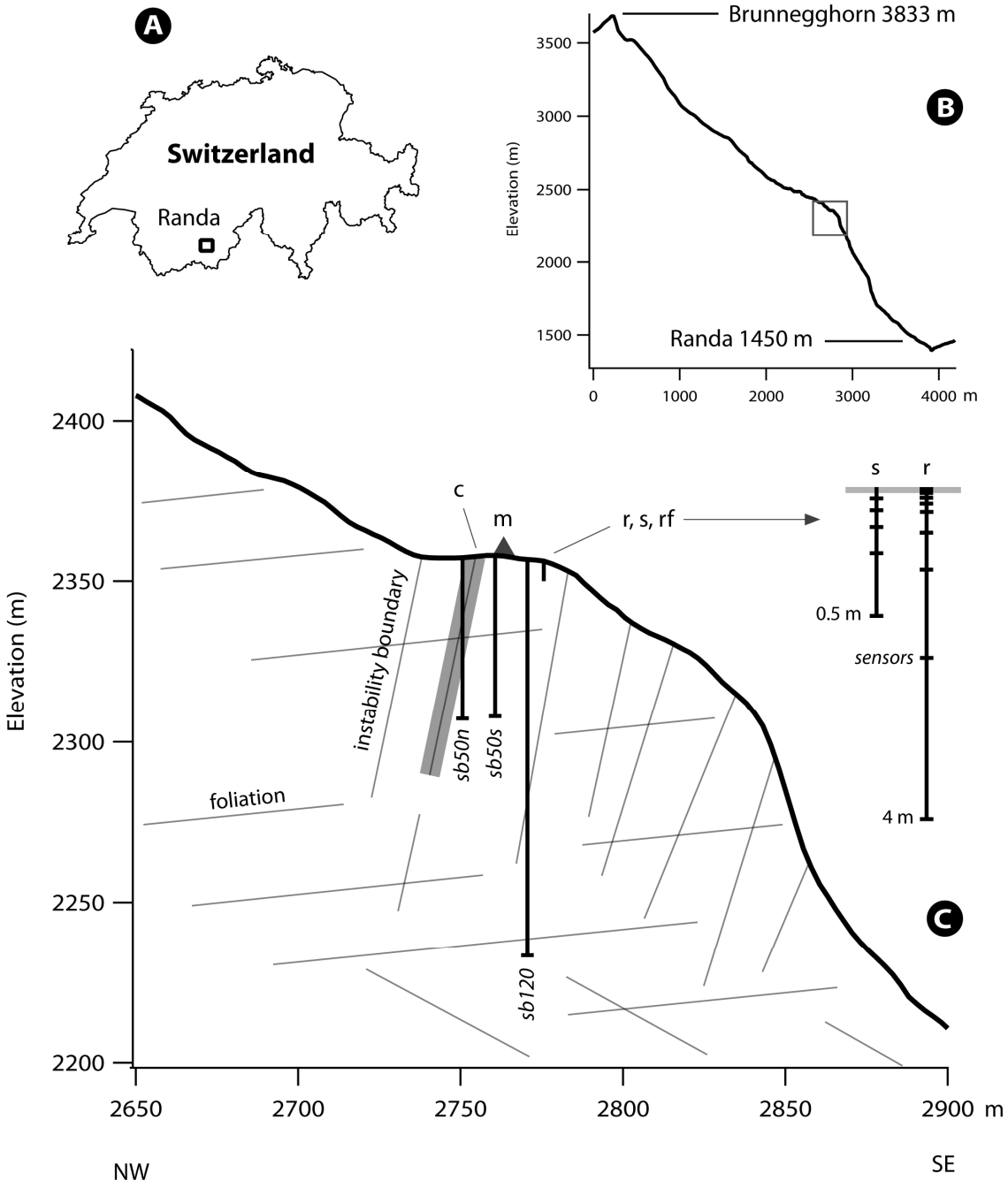

Figure 1: a) Location of the study site in Switzerland. b) Peak-to-valley profile and relative location of the monitored area. c) Overview of temperature sensors at the Randa rock slope: three boreholes each have a temperature sensor at their base, and temperature profiles were measured in sb50n and sb50s. A rock temperature array [r] contains nine sensors to 4 m depth, while an adjacent array in soil [s] consists of five sensors to 0.5 m depth. A rock face temperature sensor [rf] mimics conditions of the inaccessible scarp. Three crack temperature sensors [c] hang into an open tension crack (highlighted bold) seen to exhaust warm air in winter. A meteorological station [m] records ambient air temperature, relative humidity, and barometric pressure. An overview of main discontinuity and foliation orientations is also shown (thin gray lines).

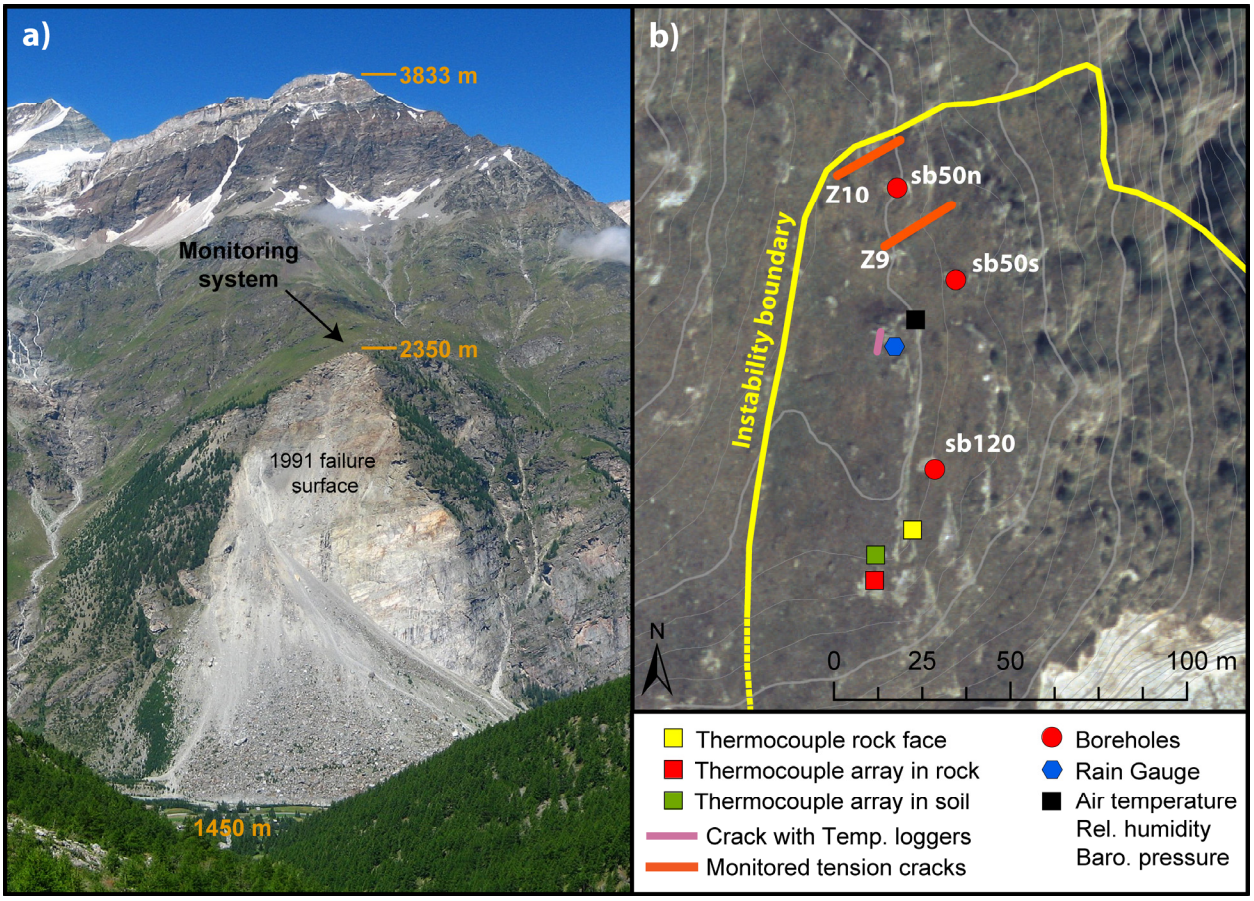

Figure 2: a) Photograph of the Randa rock slope (July 2010) showing location of the monitored area and scarp of the 1991 rockslides. b) Layout of select monitoring equipment at Randa.

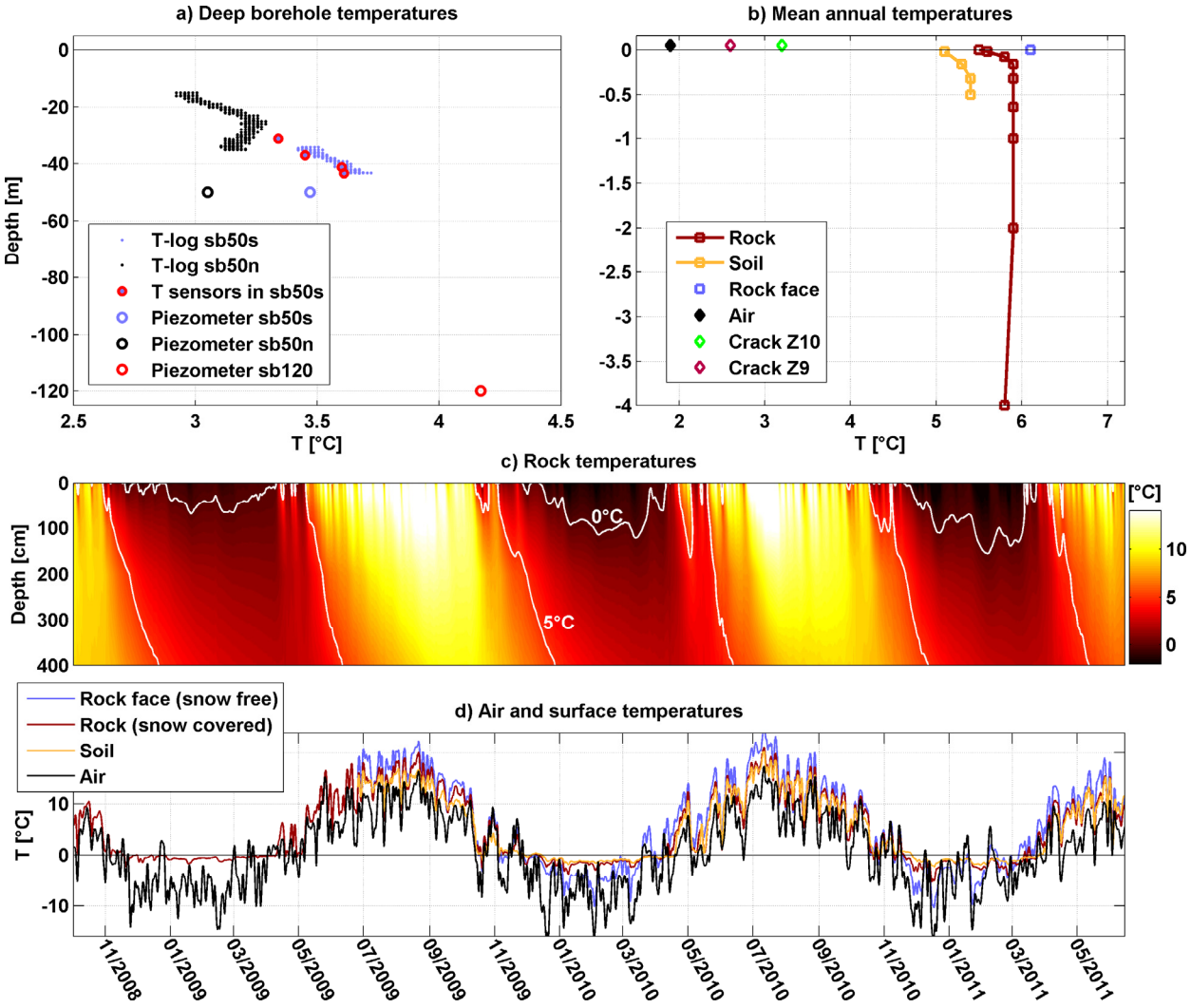

Figure 3: a) Summary of measured temperatures from boreholes sb120, sb50n, and sb50s. Data are from temperature sensors embedded in piezometers at the base of each borehole (mean values), temperature logs in water-filled portions of the 50 m boreholes (all values), and short-term continuous measurements at various depths in sb50s (mean values). b) Summary of mean annual temperatures for rock and soil arrays, vertical rock face, crack extensometers, and ambient air. c) Temperature data from the rock array plotted as a function of depth and time; data are linearly interpolated between sensor depths. d) Time series data for rock face, top of rock array, top of soil array, and ambient air temperature sensors showing variations caused by ground or snow cover and aspect, and amplitudes of annual signals. Time series in (c) and (d) are filtered with a 3-day low-pass filter.

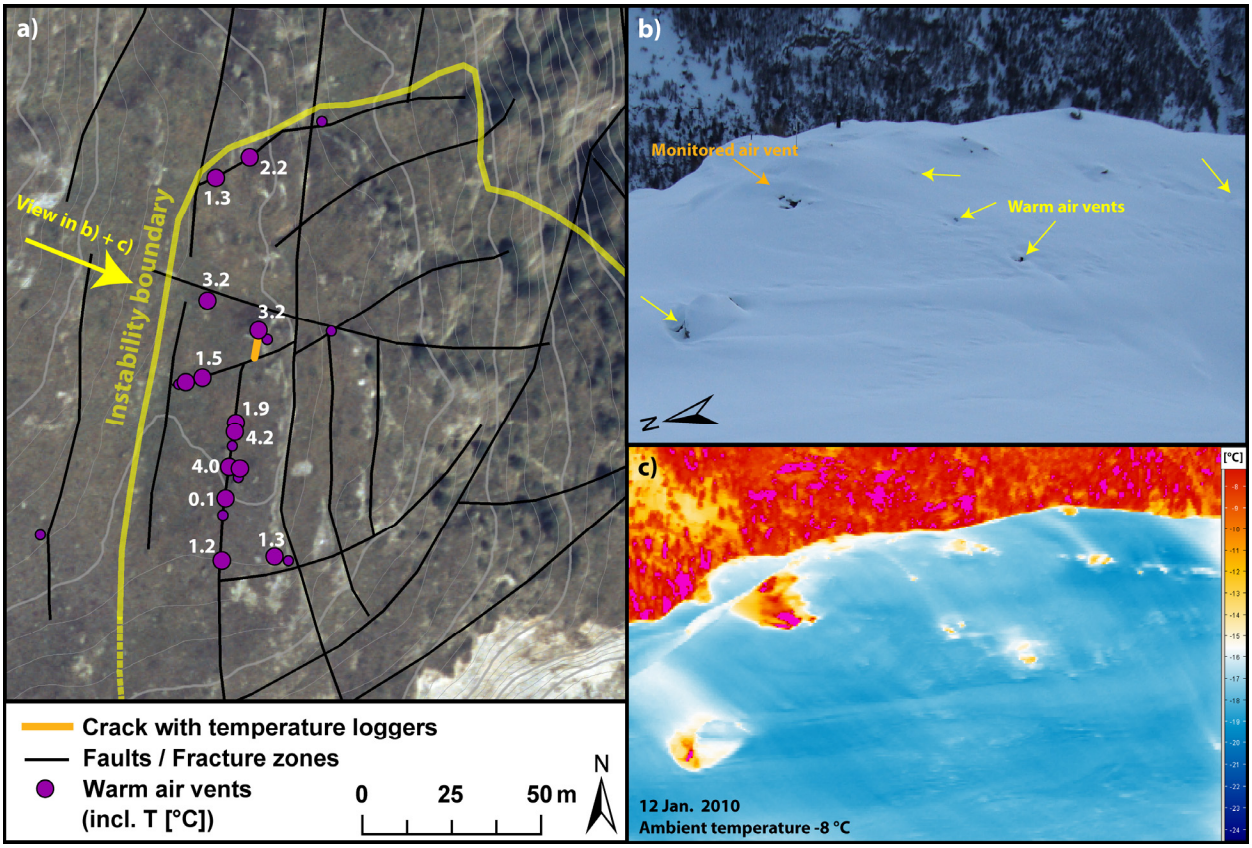

Figure 4: a) Mapped warm air vents in January 2010 shown together with measured exiting air temperature. Large-scale discontinuities traversing the slope are also shown; all air vents lie directly over open cracks, however not all open cracks have warm air vents. b) Photograph of the monitored area showing select warm air vents (see part (a) for view perspective). c) Thermal image from same perspective showing warm air exiting the vents and the presence of warm air in the surrounding snowpack. Relative temperature values are accurate, while absolute values may be offset by up to 5 °C in the uncalibrated thermal image.

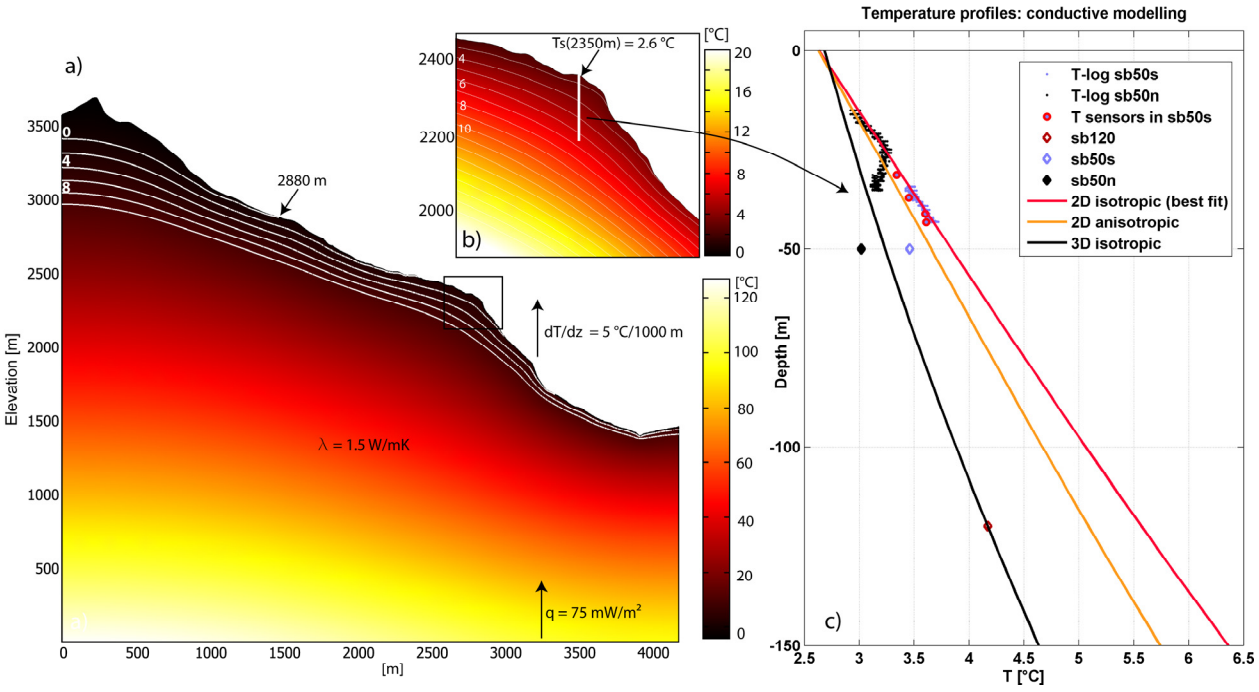

Figure 5: a) Modeled steady-state conductive temperature field for the complete mountain profile, showing implemented conductivity and boundary conditions and select isotherms. b) Detail of the monitored area showing simulated borehole where temperature profiles are extracted and compared against measured values. MGST at 2350 m is also shown. c) Modeled and measured temperatures along the simulated borehole. Shown are the best-fit results assuming 2D isotropic heat transfer, results of 2D anisotropic simulation, and the effect of implementing 3D geometry of the rock slope.

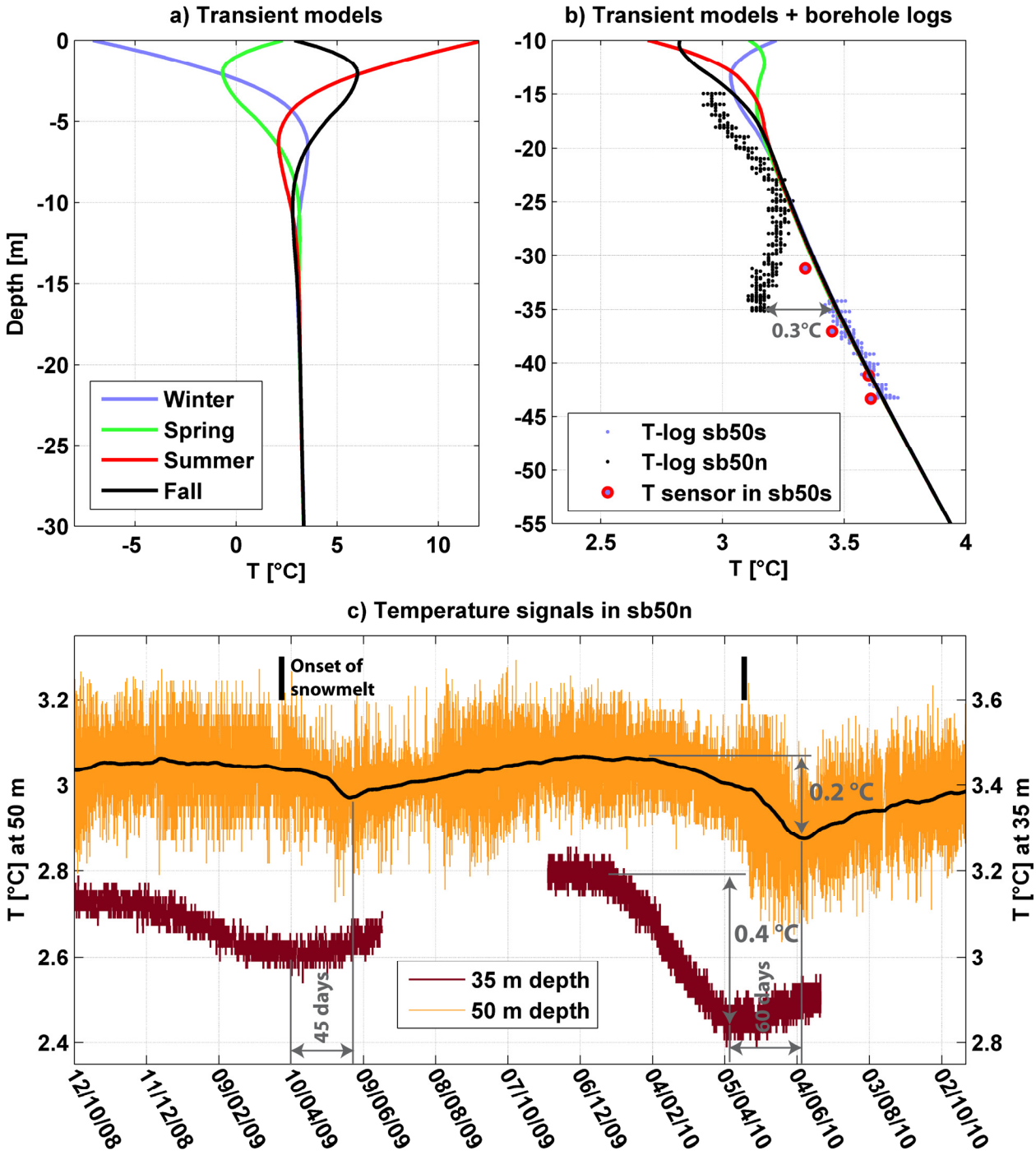

Figure 6: a) Transient ground temperature profiles for winter (Jan. 1), spring (Apr. 1), summer (Jul. 1), and fall (Oct. 1). b) Transient temperature profiles as in (a), shown with measured borehole data. Between 25 and 35 m in borehole sb50n the temperature log reverses gradient and cools; we estimate a deviation of ~0.3 °C. c) Time history data from temperature sensors at 35 and 50 m depth in borehole sb50n. Annual signals can be resolved from the two depths below the thermal active layer, with peak to peak amplitudes between 0.2 and 0.4 °C. The onset of snowmelt is indicated, as determined from the timing of water pressure increase in borehole sb50s. Time lag between minima is also noted, which together with amplitude suggest cooling closer to the upper sensor.

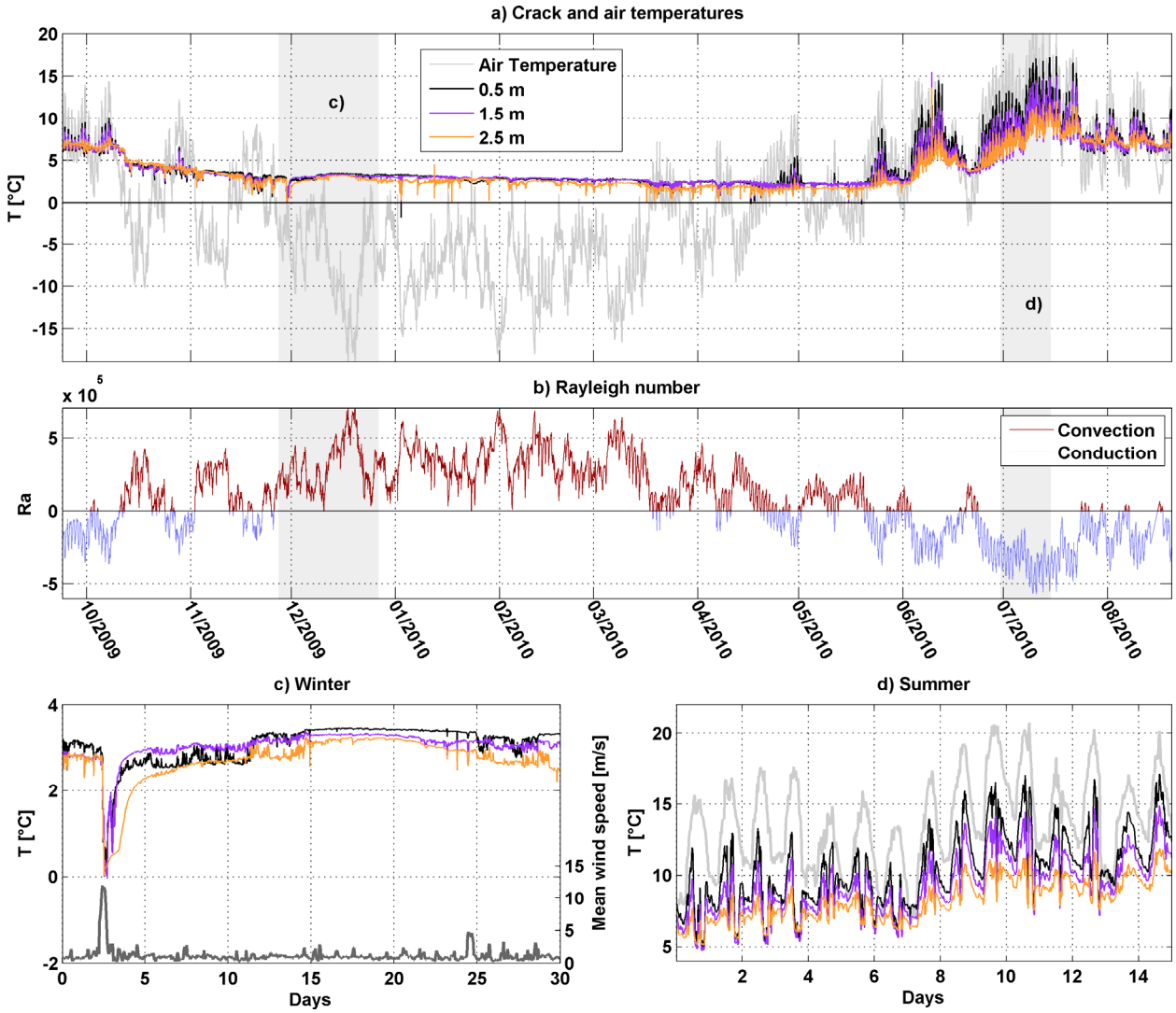

Figure 7: a) Crack and atmospheric air temperatures. b) Calculated Rayleigh number as a function of time. Rayleigh numbers exceeding the critical value indicate convection and values less than the critical suggest conduction conditions (stable air stratification) (Equation 2). Good correlation exists between the Rayleigh number and recorded temperatures: crack air temperature stabilizes under convective conditions, and follows air temperature under conductive conditions. Convection is pervasive throughout winter, during spring and fall alternating convection and conduction conditions occur, while conduction prevails in summer. c) In winter, crack air temperatures are relatively steady for nearly 8 months, decreasing gradually from ~3 to 2 °C. Steady winter temperatures are occasionally interrupted during times of high wind. d) In summer, large temperature fluctuations are observed that mimic atmospheric air temperature changes and are expected for diffusive heat transfer.

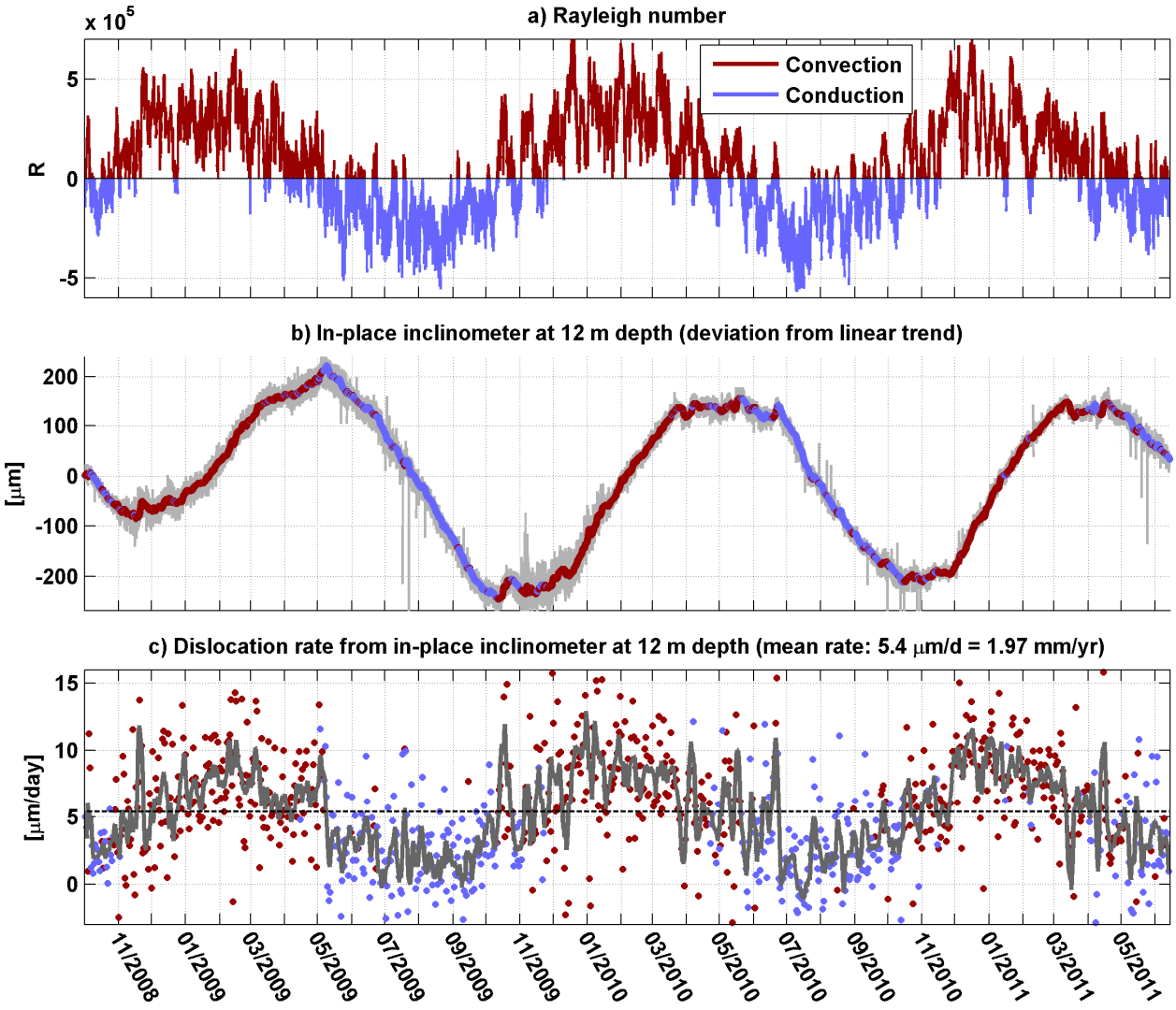

Figure 8: Comparison between a) computed Rayleigh number and b) in-place inclinometer data from 12 m depth in borehole sb120. Inclinometer measurements are low-pass filtered (original data in light gray) and the linear trend of ~2 mm/yr is subtracted to highlight annual variations; positive slopes imply a rate increase with respect to the average, negative slopes a rate decrease. Filtered data are colored according to Rayleigh number: red when convection prevails and blue otherwise. c) Daily mean deformation rate (colored points) and 5-day moving average (gray line) for inclinometer data from 12 m depth in sb120. The mean dislocation rate is also indicated (dashed line). Good correlation exists between the predicted onset or end of convective conditions and discontinuity deformation rate; the onset of convection generally brings an increase in dislocation rate, and vice versa. Convective crack air circulation may create anomalous temperature changes at depth, induced thermo-mechanical stress changes, and fracture dislocation.